eprints@whiterose.ac.uk
https://eprints.whiterose.ac.uk/

Three-Dimensional Electrical Impedance Tomography to Monitor Unsaturated Moisture Ingress in Cement-Based Materials

Danny Smyl[1] · Milad Hallaji[2] · Aku Seppänen[3] ·
Mohammad Pour-Ghaz[1]

Abstract The development of tools to monitor unsaturated moisture flow in cement-based material is of great importance, as most degradation processes in cement-based materials take place in the presence of moisture. In this paper, the feasibility of Electrical Impedance Tomography (EIT) to monitor three-dimensional (3D) moisture flow in mortar containing fine aggregates is investigated. In the experiments, EIT measurements are collected during moisture ingress in mortar, using electrodes attached on the outer surface of specimens. For EIT, the so-called difference imaging scheme is adopted to reconstruct the change of the 3D electrical conductivity distribution within a specimen caused by the ingress of water into mortar. To study the ability of EIT to detect differences in the rate of ingress, the experiment is performed using plain water and with water containing a viscosity modifying agent yielding a slower flow rate. To corroborate EIT, X-ray Computed Tomography (CT) and simulations of unsaturated moisture flow are carried out. While X-ray CT shows contrast with respect to background only in highly-saturated regions, EIT shows the conductivity change also in the regions of low degree of saturation. The results of EIT compare well with simulations of unsaturated moisture flow. Moreover, the EIT reconstructions show a clear difference between the cases of water without and with the viscosity modifying agent, and demonstrate the ability of EIT to distinguish between different flow rates.

Keywords Concrete · Electrical Impedance Tomography · unsaturated moisture transport · electrical methods · X-ray Computed Tomography

1 Introduction

The mechanical, hydraulic, chemical, thermal, and electrical properties of porous media are significantly affected by the presence of moisture (Dormieux et al (2006), Hall and Hoff (2012), Bear (1988)). For this reason, non-destructive methods of monitoring and visualizing moisture movement and distribution in unsaturated porous media are of broad interest. A variety of non-destructive techniques to visualize moisture distribution in porous media have been developed. The majority of these methods are based on electromagnetic radiation, including X-ray absorption (Hall and Hoff (2012), Pour-Ghaz et al (2009), Roels and Carmeliet (2006), Roels et al (2004), and Bauters et al (2000)), γ rays (Dierke and Werban

✉Mohammad Pour-Ghaz
E-mail: mpourgh@ncsu.edu

[1]North Carolina State University, Department of Civil, Construction, and Environmental Engineering
Campus Box 7908, 431C Mann Hall
Raleigh, NC 27695-7908
Tel.:+1 919 515 2235
Fax: +1 919 515 7908

[2]WSP USA
New York, NY

[3]Department of Applied Physics
University of Eastern Finland
Kuopio, Finland

(2013), Nizovtsev et al (2008), Nielsen (1972)), neutron imaging (Hallaji et al (2015), Zhang et al (2011), Zhang et al (2010), Kanematsu et al (2009), Zreda et al (2008), Deinert et al (2004), McCarter and Watson (1997), McCarter (1996a), McCarter et al (1996b)), and nuclear magnetic resonance (Merz et al (2014), Perlo et al (2013), Hall and Hoff (2012), Chen et al (2003), Gummerson et al (1979)). While electromagnetic radiation based methods generally provide high resolution images, these methods may be invasive, expensive, limited to testing small specimens, and/or have significant energy demand. On the other hand, electrically-based methods are generally inexpensive, non-invasive, and require comparatively lower energy (Hallaji (2015), McCarter et al (2012)).

Electrical Impedance Tomography (EIT) is an electrically-based imaging modality in which the spatially distributed electrical conductivity of a target object is reconstructed from surface electrical measurements. In porous geo-materials, EIT has recently been used to image objects buried in underwater sediment (Bouchette et al (2014)) and to monitor unsaturated moisture flow in soil (Cosentini et al (2012), Comina et al (2011), Comina et al (2010), Borsic et al (2005)) and sandstone (Stacey (2006)). In Haegel et al (2011), three-dimensional (3D) EIT was compared with magneto-electric resistivity imaging, showing the feasibility of EIT in monitoring water and air movement in sand. Further studies included solute transport in heterogeneous material within a large-scale experimental tank in (Slater et al (2002)). In geologic materials with low matrix permeability, research has included permafrost monitoring in crystalline rocks (Krautblatter and Hauck (2007)), conductive plume dilution in fractured rock environments (Nimmer et al (2007)), clay materials (LaBrecque et al (1996)), and layered formations including clay rock (Gélis et al (2010)). 3D EIT imaging has also been extended to monitor moisture and ion movement in layered soils using a time-lapse automated EIT system by Kuras et al (2009).

While the above works have shown the feasibility of EIT to visualize moisture flow and moisture distribution in geo-materials, 3D visualization of moisture flow using EIT in cement-based material has not been studied. Hydraulic and electrical properties of cement-based materials differ considerably from those of geo-materials, because of the significant differences in the microstructure of cement-based and that of geo-materials (Ulm et al (2004)). Cement-based materials generally have finer pore-size distribution and lower volumetric moisture content at saturation than many of the geo-materials tested in the previous EIT studies.

Portland cement-based materials are generally considered multiscale materials and their microstructure is often broken down into four levels. The smallest scale, commonly referred to as Level 0, which is above the atomic scale, ranges from 10^{-10} to 10^{-9} m. The structure at this scale is made of calcium silicate hydrate solid (C-S-H solid) with a characteristic length of 5.6 nm and 18% porosity. At a level above the Level 0, Level I, encompassing length scales below 10^{-6} m, C-S-H solid and gel porosity form the so-called C-S-H phase with porosity ranging from 24 to 37% and characteristic length of 16.6 nm. Level II ranges from $10^{-6} - 10^{-4}$ m to and consists of C-S-H phase, unhydrated cement particles, calcium hydroxide crystals, aluminate phases, and capillary porosity. The volume of capillary porosity is dependent on the initial water-to-cement ratio (w/c) and the degree of hydration (extent of chemical reaction). In well-hydrated low w/c ratio system, generally below w/c = 0.42 in Portland cement-based materials, capillary porosity can be negligible, and in high w/c ratio systems with a low degree of hydration it can be a significant portion of the volume. For example at w/c = 0.60 with 50% degree of hydration, volume of capillary porosity is approximately 45% of the cement paste volume. Finally, Level III has a characterization length larger than 10^{-3} m. Level III describes mortar and concrete materials as composite materials consisting of cement paste, fine aggregate, coarse aggregate, and interfacial transition zone (ITZ). ITZ refers to the region in the immediate vicinity of the aggregate that can have properties different from that of bulk cement paste. We note there that the above description of microstructure follows the description by (Dormieux et al (2006), Jennings (2000), and Richardson (1999)).

The resolution of imaging modalities, specifically electromagnetic-based modalities, to capture microstructure features depends on many factors including the type of electromagnetic field, available energy, and the attenuation of the target. In X-ray computed tomography (CT), the resolution of the scanners range from very high resolution (synchrotron-based micro CT, 5-20 μm), intermediate resolution (medical scanners, 100 - 500 μm), to lower resolution scanners ($\approx 400\mu$m) (Wildenschild et al (2002)). In application to cement-based materials, these modalities can be used to probe mainly Level II and III microstructure with grain sizes ranging from $10^{-6} - 10^{-3}$ m. X-ray radiography and tomography however are not a very powerful methods for monitoring moisture ingress in cement-based materials and can only provide information about the high moisture content regions in cement-based materials.

Neutron tomography commonly reports image resolutions of on the order of 50 μm (Woracek et al (2014), Vontobel et al (2005)). Recently, Hallaji et al (2015) used neutron radiography with 30 μm resolution. Therefore, neutron tomography can be used to probe Level II and III microstructure, similar

to X-ray tomography. It should be noted, however, that neutron tomography is generally well-suited for moisture flow monitoring due to the high neutron cross-section of hydrogen. The ability of neutron tomography to capture moisture flow in geophysical applications was shown in Masschaele et al (2004). Tomography and radiography using γ radiation is less common than X-ray and neutron methods, with a resolution of ≈ 0.1 mm (Pires et al (2005), Duliu et al (2003)).

The resolution (or the so-called distinguishability in Isaacson's sense (Isaacson (1986))) of EIT is a function of many factors such as geometry and size of the target, prior information, mesh size, current injection pattern, presence of noise, and measurement resolution. EIT, generally, has lower spatial resolution than electromagnetic radiation based tomographic methods due to the diffusive nature of electricity. EIT, however, has been shown to be a powerful modality in monitoring moisture flow in soil and cement paste (Smyl et al (2016), Hallaji et al (2015), Looms et al (2008)).

Daily and coauthors (Daily et al (1994), Buettner et al (1996a), and Buettner et al (1996b)) were perhaps the first to study the feasibility of EIT to monitor moisture transport in cement-based materials. They used simple two- and four-point measurement schemes in 2D geometries. However, their results were not corroborated and their reconstructions provided low spatial resolution. Recently, EIT was used to monitor 1D moisture flow in concrete slabs (Du Plooy et al (2015)). The EIT reconstructions were compared against Ground Penetrating Radar (GPR) results. In a more recent work, Hallaji et al (2015) studied imaging of 2D moisture flow in cement paste containing no aggregates, and compared EIT reconstructions with Neutron Radiography images, showing a good agreement between the two imaging methods. These studies have shown the potential of EIT to be used as a non-destructive, non-invasive means of monitoring moisture flow in cement-based materials.

In the present work, we expand upon the previous work by Hallaji et al (2015) and attempt to answer the open research question at the end of their article: Can EIT be used to monitor 3D moisture flow in cement-based materials containing aggregates? To answer this question, we conduct an experimental study of imaging 3D moisture flow in cement-based mortar containing fine aggregates. To corroborate the EIT reconstructions, X-ray CT images and 3D simulations of unsaturated moisture flow are compared with the EIT reconstructions. We also investigate whether EIT has adequate sensitivity to detect the difference between flow rates of fluids with differing viscosity and surface tension (resulting from the addition of radiocontrast agent, Iohexol).

In the following sections of this paper, materials and sample preparation are presented, a brief review of the difference imaging scheme in EIT is provided, the EIT experimental measurement strategy is presented, the numerical method of simulating unsaturated moisture flow in cement-based material is discussed, and an overview of the X-ray CT imaging method used here is provided. Finally, in Results section, the EIT reconstructions corresponding to ingresses of water without and with the viscosity/surface tension modifying agent are illustrated, and compared with X-ray CT images as well as moisture transport simulations.

2 Materials and sample preparation

2.1 Fluids in the absorption test

In the experiments, two liquids were used: plain water and water with radiocontrast agent (Iohexol solution, diluted to 120 mg Iodine/ml). Iohexol was chosen as an additive to water because it is effective in improving the contrast in X-ray Computed Tomography images, which was used as experimental corroboration with EIT in this work. It should be noted that trial experiments using plain water were performed, and water ingress was not observable with CT. Iohexol increases fluid surface tension and viscosity when added to water (Iohexol has surface tension and viscosity of 86.6 dyne/cm and of 2.3×10^{-3} Pa·s at 25°C, while values of water are 71.9 dyne/cm and 8.9×10^{-4} Pa·s at 25°C). In cement-based materials, increasing both the surface tension (γ) and viscosity (μ) has been shown to change the rate of absorption proportional to $\sqrt{\frac{\gamma}{\mu}}$ (Spragg et al (2011)). Therefore, water containing Iohexol was expected to penetrate the mortar specimen at a different rate than plain water. To confirm this, a sorption experiment was conducted.

2.2 Preparation of EIT and sorption test specimens

The specimens in the EIT and CT experiments were made of mortar, consisting of cement paste and fine aggregates. Ordinary Portland cement (OPC, Type I) and fine aggregate consisting of non-angular

siliceous natural river sand with a fineness modulus of 2.63 and maximum aggregate size of 2 mm were used. A high w/c ratio and low volumetric aggregate content ($v_a = 40\%$) were used to increase material porosity and permeability to accelerate the rate of moisture ingress and reduce the X-ray CT testing duration. The porosity of the cement paste, ϕ_p, may then be estimated using $\phi_p = \frac{\theta_s}{1-v_a}$, where θ_s is open porosity further discussed in Section 3.2. The mixing was carried out according to ASTM C192-06 (ASTM (2006)) and two cylinders with diameter 10.20 cm and height 20.30 cm were cast. The cylinders were demolded after 18 hours and cut in half horizontally using a wet-saw to create the specimens used in EIT and CT testing.

Since the specimens were saturated after demolding at 18 hours, they were moved to an oven at $50°C$ for 5 hours to reduce their moisture content. The specimens were then sealed in two layers of plastic bags and placed inside an environmental chamber at $23°C$ for 21 days. This conditioning process was carried out to achieve a relatively uniform moisture content throughout the specimen. It should be noted that uniform moisture content is not necessary for EIT. The above conditioning resulted in an initial volumetric moisture content, $\theta_i = 0.07$, which was determined experimentally by completely drying a set of identically conditioned specimens of the same material and geometry. A summary of material properties are provided in Table 1.

Table 1 Material and hydraulic parameters

w/c	$v_p\,(\frac{mm^3}{mm^3})$	$\phi_p\,(\frac{mm^3}{mm^3})$	$K_s\,(\frac{mm}{hr})$	$\theta_s\,(\frac{mm^3}{mm^3})$	$\theta_i\,(\frac{mm^3}{mm^3})$	$\theta_r\,(\frac{mm^3}{mm^3})$	$I\,(-)$	$\alpha\,(\frac{1}{mm})$	$n\,(-)$
0.60	0.40	0.25	0.005	0.15	0.07	0	-9.0	0.026	1.77

For the sorption experiments that were used for studying the effect of Iohexol on the absorption rate of water, two cylinders with diameter and height of 5.0 cm were cast. The material was the same and the sample preparation procedure was similar to the specimens used in EIT and CT testing. However, unlike the EIT/CT specimens, the sorption test specimens were cast in PVC pipes and oven dried at $50°C$ for 24 hours after the 21 days of initial curing. Complete desaturation was selected as the initial condition to minimize moisture gradient in the specimen and to maximize the amount of absorbed fluid. It should be noted that since the only purpose of the sorption experiment was to verify that the addition of Iohexol reduces the rate of absorption, the initial condition was not a critical parameter. Sorption tests were carried out for 22 hours.

2.3 Preparation of electrodes and water reservoir

The electrodes used in EIT measurements were made of colloidal silver paint. The silver paint had a viscosity of 10 Pa·s, a pH between 10.0 - 10.5, and a dried electrical resistivity of $1.60 \cdot 10^{-8}\ \Omega \cdot m$ (MSDS (2016)). This paint has a low resistivity and is fast drying, making it a suitable material for "painted" electrodes (Pour-Ghaz (2011)). It has been shown in (Pour-Ghaz (2011), Pour-Ghaz and Weiss (2011), Raoufi et al (2011), Weiss and Pour-Ghaz (2011), Ford et al (1998)) that the use of fast-drying colloidal silver paint reduces contact impedance compared to conventional electrodes (i.e. copper foil or metallic sheets). Since the silver paint dries rapidly (on the order of a few seconds), the penetration into the immediate pore system is negligible. Especially, in this work, the dimensions of specimens are orders of magnitude larger than the potential penetration depth of the paint, reducing the potential influences on the measurements. In addition, this work employs the difference imaging scheme where the effect of electrode contact impedance is largely subtracted between the two sets of measurements.

A total of 24 square shaped electrodes (with dimension of 1.3 cm × 1.3 cm) were painted on the side surface of the cylindrical specimens using a small brush. The electrodes were arranged in three equally spaced 8-electrode rings. Figure 1b shows the specimen and the locations of the electrodes. After the silver paint electrodes had dried, an 18-gage wire was attached to each electrode using an electric tape, and its contact was secured using a zip tie.

The slight variations in electrode sizes and shapes, in principal, introduces measurement and modeling errors. In addition, there are multiple contacts in this experimental setup, namely, sliver paint/sample and wire/silver paint electric contacts that can affect the results. The contact impedance of the silver paint/sample is the most important contact impedance that needs to be properly accounted for in modeling (the copper wire to silver electrode contact impedance is very small since both materials are very

conductive). Once more, since difference imaging is used, much of the systematic experimental and modeling errors cancel. It should also be noted that the length of the wires can also affect the measurements. In this work the length of wires was cut to the minimum length required to reach the specimen from the EIT equipment. In addition, the frequency of the measurements is relatively low and the measurements are not significantly impacted by the length of the wires.

To facilitate absorption, a water reservoir made of PVC was mounted on the top surface of each specimen using silicon caulking. The silicon caulking was fast-drying and had a very high viscosity (as compared to water), which minimized its penetration into the specimen. Moreover, it can be seen in the X-ray CT images (Section 4), where the silicon showed significant contrast to the mortar, there was minimal penetration into the specimen. The length and internal diameter of the PVC pipe was 5.0 cm and 0.95 cm, respectively, and it was positioned eccentrically 1.3 cm off-center. After placing the water reservoirs, the mortar cylinders were wrapped with transparent tape to prevent evaporation of water from the specimens' surface during the experiment (Fig. 1a). To minimize evaporation from sample during the test, the exterior of the specimen and around the base of the water reservoir was sealed with two layers of transparent plastic tape.

3 Methods

In the experiments, water without and with the radiocontrast agent was let to ingress each mortar specimen from a water reservoir (See Section 2.3 and Fig. 1a). EIT measurements and CT scanning were both carried out at several time intervals during the absorption of moisture. The EIT and CT measurements were also collected prior to the addition of the solution to the reservoir ("reference measurement," see below). The experimental results were corroborated with a numerical simulation of unsatured moisture flow. The methods used in the study are described in this section.

3.1 Electrical impedance tomography

3.1.1 Imaging Scheme

In EIT, a series of electric currents are injected between pairs of electrodes at the surface of a target and corresponding to each current injection, the electrical potential differences (voltages) between multiple electrode pairs are measured. In general, the same set of boundary electrodes is used for current injections and potential measurements. Based on these measurements, the spatial distribution of the electrical conductivity inside the object is reconstructed. Mathematically, the reconstruction problem in EIT is a non-linear ill-posed inverse problem, in the sense that its classical solutions are non-unique and very sensitive to modeling errors and measurement noise.

A variety of computational methods for image reconstruction in EIT have been developed (Borcea (2002)). In a broad sense, the reconstruction methods can be categorized as *absolute* and *difference* imaging. In absolute imaging, the distribution of electrical conductivity is reconstructed based on a single set of potential measurements during which the object is assumed to be non-varying. Absolute imaging often necessitates iterative solution of the nonlinear EIT problem. In difference imaging, the change in the conductivity between two states is reconstructed from potential measurement data corresponding to these two states. In this paper, the conductivity changes in a specimen at different stages of moisture ingress are reconstructed using difference imaging.

The inverse problem of EIT requires a forward model. The most accurate known forward model for the EIT measurements is the Complete Electrode Model (Cheng et al (1989), Somersalo et al (1992)). The CEM consists of the partial differential equation

$$\nabla \cdot (\sigma \nabla u) = 0, \quad x \in \Omega \tag{1}$$

and the boundary conditions

$$u + \xi_l \sigma \frac{du}{dn} = U_l, \quad x \in e_\ell, \ \ell = 1, \dots, L \tag{2}$$

$$\sigma \frac{du}{dn} = 0, \quad x \in \partial\Omega \backslash \bigcup_{\ell=1}^{L} e_\ell \tag{3}$$

$$\int_{e_l} \sigma \frac{du}{dn} \, dS = I_l, \quad \ell = 1, \ldots, L \tag{4}$$

where Ω is the target volume, $\partial\Omega$ is its boundary, σ is the electrical conductivity, u is the electric potential, n is the unit normal, e_l is the lth electrode, and ξ_l, U_l and I_l, respectively, are the contact impedance, electric potential and total injected current corresponding to e_l. Moreover, the current conservation law must be fulfilled

$$\sum_{l=1}^{L} I_l = 0 \tag{5}$$

and the potential reference level must be fixed

$$\sum_{l=1}^{L} U_l = 0. \tag{6}$$

To approximate the solution of the CEM for an object with arbitrary geometry, a numerical method is necessary. In this work, Finite Element Method (FEM) is employed (Vauhkonen et al (2001)). The FEM approximation of the forward model used in this work follows the well-known implementation of the variational equation (Vauhkonen et al (1999)). The meshing of the domain is detailed later in this section.

In difference imaging, the change in electrical conductivity ($\delta\sigma$) from a reference conductivity state (σ_o) to the current state of conductivity, (σ), is reconstructed (i.e., $\delta\sigma = \sigma$ - σ_o). A global linearization approach using a Taylor Polynomial at σ_o is used such that

$$U(\sigma) = U(\sigma_o) + J[\sigma - \sigma_o] + O(||\sigma - \sigma_o||^2) \tag{7}$$

where $U(\sigma)$ is the finite element approximation of the mapping between the discretized conductivity σ and a vector consisting of electrode potentials, $J = \frac{dU}{d\sigma}(\sigma_o)$ is the Jacobian matrix at σ_o, and $O(||\sigma - \sigma_o||^2)$ denotes the higher-order terms. When the higher-order terms are neglected and the observation noise accounted for, the observation model for $\delta V = V - V_o$, the difference between measurement realizations V and V_o corresponding to states σ and σ_o, can be written as

$$\delta V \approx J\delta\sigma + \bar{v} \tag{8}$$

where $\delta\sigma = \sigma - \sigma_o$ is the change in the conductivity, and $\bar{v}$ is the difference between randomly-distributed observation noises in the two sets of measurements.

In Eq. (8), the measured potential difference between the two states, δV, is linearly related to the conductivity change, $\delta\sigma$, using a global linearization at an estimated reference state σ_o. This has a few consequences: (i) since the potential difference between two states is considered, some of the modeling errors and/or *systematic* measurements errors that exist in both measurement sets may cancel out. This makes difference imaging a rather tolerant imaging scheme to systematic modeling or measurements errors. (ii) Since the nonlinear problem is globally linearized, the solution does not require iterations, and the computational cost of the reconstruction decreases. (iii) Due to the global linearization, the computed changes in conductivity do not necessarily reflect the actual conductivity changes. This is especially true if the changes in conductivity are large. This makes the results of difference imaging *qualitative* (Vauhkonen (2004)). (iv) Difference imaging may fail to provide reasonable solution if the change in conductivity with respect to reference state is very large (Hallaji et al (2014)). (v) If the linearization point, σ_0, is far from the actual conductivity of the reference state, results may be unreasonable. In general, difference imaging is a powerful tool when the primary interest is to observe the location and approximate change in electrical conductivity.

Due to the ill-posed nature of the EIT inverse problem, solving the conductivity change $\delta\sigma$ from Eq. (8) in the least squares sense would yield non-unique and unstable solutions (Vauhkonen et al (1998)). Therefore, regularization is needed. In generalized Tikhonov regularization (Tikhonov and Arsenin (1977)), the solution of the (linearized) inverse problem is written in the following form

$$\widehat{\delta\sigma} = \arg\min_{\delta\sigma} \left\{ ||\delta V - J\delta\sigma||^2 + p_{\delta\sigma}(\delta\sigma) \right\} \tag{9}$$

where $p_{\delta\sigma}(\delta\sigma)$ is a side constraint term which regularizes the solution (Heidary-Fyrozjaee (2008), Beck and Ben-tal (2006)). In this paper, $p_{\delta\sigma}(\delta\sigma)$ is chosen to be of the form $p_{\delta\sigma}(\delta\sigma) = \alpha||L_{\delta\sigma}\delta\sigma||^2$, where L is a first order discrete differential operator and α is a regularization parameter which controls the weight

of the side constraint in the solution. Such a choice of $p_{\delta\sigma}(\delta\sigma)$ is known to promote spatial smoothness in the solutions; smoothness promoting regularization is particularly well-suited for diffusive processes, such as moisture ingress (Liu et al (2014)), and was used also by Hallaji et al (2015). For alternative choices of $p_{\delta\sigma}(\delta\sigma)$, see e.g. Kaipio and Somersalo (2005).

In this work, MATLAB implementation of (Adler and Lionheart (2006), Polydorides and Lionheart (2002)) was used. A total of 828,188 quadratic 10-node tetrahedral elements with a maximum element dimension of 2.0 mm were used in discretization of the domain. The mesh (shown in Figure 2) was generated using Delauney meshing and application of NetGen (Schöberl (1997)). The meshing on and near the electrodes used the same meshing criteria as the elements within the modeled specimen. Further, the six nodes used on the electrode surface correspond to the nodes on the side of the same tetrahedral element within the specimen volume. The modeling of the electrodes approximated the contact impedance as 0.01. We would like to point out that due to the use of the difference imaging scheme, in general, the value of contact impedance does not affect the reconstructions since its effect is subtracted between the two sets of measurements.

3.1.2 EIT measurement strategy

The EIT measurements were carried out using an in-house developed EIT equipment described in Hallaji et al (2015). In all measurements, an alternating current with 0.10 mA amplitude and 40 kHz frequency was used. This frequency was chosen based on Electrical Impedance Spectroscopy (EIS) measurements; at frequency 40 kHz, the imaginary component of the impedance was at the minimum. The accuracy of the potential measurements was $\pm 1.0 \times 10^{-8}$ V. The current injection pattern consisted of: (i) injecting current between electrode pairs (i, j) on the same ring of electrodes $i = 1 \ldots 8, 9 \ldots 16, 17 \ldots 24$ and $i, j = 1 \ldots 8, 9 \ldots 16, 17 \ldots 24$ and $i \neq j$, (ii) between electrode pairs (k, l) located on different rings of electrodes $k = 1, l = 9 \ldots 16$ and $k = 8, l = 17 \ldots 24$, and $k = 1, l = 17 \ldots 24$. Corresponding to each current injection, potential measurements were taken with respect to a common ground. Electric potential differences were only considered between adjacent electrodes on the same ring level. This current injection and potential measurement protocol resulted in 561 current injections and 4488 potential measurements for each set of EIT measurements. The sampling frequency was automated in the EIT equipment, which was a function of the excitation frequency.

3.2 Numerical simulation of unsaturated moisture transport

3.2.1 General

The isothermal unsaturated moisture transport in porous media was simulated using Richards' Equation (Richards (1931)):

$$\frac{\partial \theta}{\partial t} = \frac{\partial}{\partial x}\left(K(h)\frac{\partial h}{\partial x}\right) + \frac{\partial}{\partial y}\left(K(h)\frac{\partial h}{\partial y}\right) + \frac{\partial}{\partial z}\left(K(h)\frac{\partial h}{\partial z} + 1\right) \tag{10}$$

where $K = K(h)$ (mm/hr) is the unsaturated hydraulic conductivity, $\theta(\text{mm}^3/\text{mm}^3)$ is the volumetric moisture content, $h(\text{mm})$ is the pressure head, x, y, and z are the spatial coordinates (Pour-Ghaz et al (2009)). In classical Richards' Equation, air diffusion and dissolution are neglected. In this work, a finite element approximation of Eq. (10) was used to simulate moisture flow in mortar.

3.2.2 Material model

In general, the unsaturated hydraulic conductivity is expressed as the product of the relative hydraulic conductivity K_{r}, and the saturated hydraulic conductivity K_{s}, $(K = K_{\text{r}}K_{\text{s}})$. For unsaturated porous media, Mualem's equation (Mualem (1976)) is used to describe K_{r}

$$K_r = \Theta^I \left[\frac{\int_0^\Theta \frac{1}{h(x)}, dx}{\int_0^1 \frac{1}{h(x)}, dx}\right]^2 \tag{11}$$

$$\Theta = \frac{\theta - \theta_{\text{r}}}{\theta_s - \theta_{\text{r}}} \tag{12}$$

where $0 \leq \Theta \leq 1.0$ is the effective material saturation, and θ_{r} is the residual moisture content; $\theta_{\mathrm{r}} = 0$ is generally considered as an appropriate assumption for cement-based materials (Pour-Ghaz et al (2010), Pour-Ghaz et al (2009)). Moreover, θ_{s} is the saturated water content that was determined experimentally in this work), I is the tortuosity and pore connectivity parameter and in this work I was taken from Smyl et al (2015). Further discussion of I in cement-based materials is provided in Auroy et al (2015) and Poyet et al (2011). In this work, K_{s} was determined experimentally using Darcy's Law and the procedure in Ghasemzadeh and Pour-Ghaz (2014).

In order to calculate the integrals in Eq. (11), the effective material saturation was expressed as a function of the pressure head, $\Theta = \Theta(h)$ using the van Genuchten model (van Genuchten (1980), van Genuchten and Nielson (1985)):

$$\Theta = \frac{1}{[1 + (\alpha h)^n]^m}, \quad m = 1 - \frac{1}{n} \tag{13}$$

where $\alpha(\mathrm{mm}^{-1})$ and $n(-)$ are fitting parameters. For cement-based materials, instead of expressing water retention as $\Theta = \Theta(h)$, the material sorption isotherm is generally obtained experimentally as $\Theta = \Theta(RH)$, where RH denotes relative humidity. In this work, the desorption isotherm was experimentally determined using an automated sorption analyzer (Villani et al (2014), Pour-Ghaz et al (2010)). It should be noted that in the present work we neglected the hysteresis effect for simplicity. To convert the experimentally obtained isotherm $\Theta(RH)$ to the moisture retention curve as $\Theta(h)$, the Kelvin-Laplace Equation was used (Pour-Ghaz et al (2009), Leech et al (2008)):

$$h = \frac{\rho_{\mathrm{w}} RT}{m_{\mathrm{w}}} \ln(RH) \tag{14}$$

where ρ_{w} (g/mm^3) is the density of water, R (8.845JK^{-1}mol^{-1}) is the universal gas constant, and m_w (g/mol) is the molecular weight of water. By fitting the model in Eq. (13) to the water retention curve $\Theta(h)$, van Genuchten parameters α and n were obtained. A summary of the hydraulic properties are provided in Table 1. Figure 3 shows the fitted van Genuchten model and experimentally obtained data points.

3.2.3 Simulation of moisture flow

The moisture flow in the specimen was simulated using a commercially available Finite Element Software HYDRUS 3D (Šimůnek et al (2008)). The finite element scheme was solved using the Galerkin formulation of Richards Equation with linear basis functions. Zero-flux boundary conditions were considered at all surfaces except for the surface from which water penetrated (area under the water reservoir), which was modeled as a 9.5 mm diameter circle saturated throughout the simulation. Uniform initial moisture content, $\theta_i = 0.07$ was considered as discussed in Section 2. The finite element mesh consisted of linear tetrahedral elements with four nodes and a maximum dimension of 4 mm, a total of 124,138 elements were used in the simulation. The finite element model was solved in terms of moisture content and the preconditioned conjugate-gradient method was used to solve the resulting systems of equations. The mesh, with the same dimensions of the EIT specimen is shown in Figure 4.

3.3 X-ray CT imaging

To corroborate EIT reconstructions, X-ray Computed Tomography (CT) imaging was conducted using a full-scale medical CT scanner with a peak beam energy of 120 kV and intensity of 40-200 mA (see Fig. 5). In the CT scanner, the X-ray tube rotates perpendicular to the circular cross-section of the specimen. As the fan beam rotates around the specimen, detectors on the opposite side are activated and measurements are taken. Upon completing a full rotation, the X-ray absorption coefficient, $\mu(\mathrm{mm}^{-1})$, is computed in voxels within the measured slice. X-ray radiation transmitted through the specimen is related to μ via the Lambert-Beer law:

$$I_{\mathrm{x}} = I_0 \exp(- \int \mu d\ell) \tag{15}$$

where I_{x} is the intensity of the transmitted X-ray passing through the specimen, I_0 is the incident X-ray intensity, and $d(\mathrm{mm})$ is the specimen thickness which is computed during the reference CT scan. The

voxel values of the CT images, $\mu - \mu_{\text{water}}$, were normalized by $\mu_{\text{water}} - \mu_{\text{air}}$ to get Hounsfield numbers H is defined by (Feeman (2010)):

$$H = 1000 \times \frac{\mu - \mu_{\text{water}}}{\mu_{\text{water}} - \mu_{\text{air}}}. \tag{16}$$

.

Further, the spatial distribution of volumetric moisture content, θ, was computed from the Hounsfield numbers (Tiana et al (2007)):

$$\theta = \frac{H_{\text{s}} - H}{1000}. \tag{17}$$

where H_{s} is the Hounsfield value of a saturated material. Here, the value of H_{s} was taken from H values corresponding to voxels directly below the water reservoir, where the material was assumed to be completely saturated.

The specimen was scanned at time intervals of 30 minutes, 1, 2, 7 and 22 hours. Since testing was conducted medical facility, access of to the scanner was limited to normal business hours. Therefore, testing was conducted continuously for 7 hours and then once again during normal business hours the following day. 2D slices were taken through the horizontal and vertical cross sections in 0.6 mm slices. CT images were analyzed using digital imaging software (Abramoff et al (2004)). We would like to note that the silver electrodes diffracted X-rays during the scanning, however the diffraction was minimal and did not impact the image analysis.

4 Results and discussion

Figure 6 shows the results of the experiment, where water with radiocontrast agent (Iohexol) was absorbed to a specimen. The left column of the figure shows 2D slices of the 3D EIT reconstructions corresponding to 30 minutes, 1, 2, 7, and 22 hours of moisture ingress, and on the right column, the respective CT images are depicted. The planes of the vertical 2D slices pass through the center of the water reservoir, extending to the sides of the specimen[1]. The rectangles in the EIT images illustrate the locations of electrodes. It should be noted that the EIT images represent the change in the electrical conductivity, $\delta\sigma$ (mS/cm), because the difference imaging scheme was used, as discussed in Section 3.1, while the CT images show the volumetric moisture content, θ, computed using the procedure in Section 3.3. The relationship between volumetric moisture content, θ, and electrical conductivity, σ, is highly nonlinear for cement-based materials. Therefore, the comparison between the left and right column in Figure 6 is only qualitative.

X-ray CT images and EIT reconstructions do not compare well: The CT shows the change of the moisture content, θ, only in a small area below the water reservoir, while EIT images imply deeper penetration of moisture. Indeed, after 22 hours of moisture ingress, the conductivity distribution has changed in a volume extending to more than half of the specimen height. Moreover, the EIT images show more distinct variability in $\delta\sigma$ than CT shows in θ. These qualitative differences between CT and EIT images are results of CT being capable of showing only high degrees of saturation. This conclusion is in agreement with the previous study by Pour-Ghaz et al (2009) in which X-ray radiography could only detect areas with moisture content close to saturation and the gradient of moisture content was not observable in a small square sample with dimensions 25.4 mm × 25.4 mm and 6.35 mm thick. Observing the gradient of moisture content in cement-based samples using X-ray radiography and X-ray CT is even more difficult in larger samples (Roels and Carmeliet (2006), Roels et al (2004)). The result of this experiment demonstrates that EIT has potential for (at least qualitatively) imaging the unsaturated moisture flow in large dimensional objects made of cement-based material – in conditions where standard medical X-ray CT scanners fail.

Since CT images did not capture low levels of moisture content, simulation of unsaturated moisture flow was selected as an additional corroboration method for EIT results. Figure 7 shows 2D slices of 3D EIT reconstructions of water penetration *without Iohexol* (left column) and 2D slices of 3D numerical simulations of unsaturated moisture flow (right column). This comparison of simulation results reporting quantitative volumetric moisture content, θ, to EIT reconstructions of $\delta\sigma$ is again qualitative due to the difference imaging approach. Nevertheless, the spatial distributions of $\delta\sigma$ and θ compare well at times from 30 minutes to 7 hours. The EIT reconstruction corresponding to 22 hours of moisture penetration shows large artifacts, which is discussed later in this section.

---

[1] X-Ray CT images show the water reservoir at the center of the specimen due to the orientation of the sample during testing (shown in Fig. 5).

We would like to add that a comparatively lower number of elements were used in moisture flow simulations as compared with EIT reconstructions (elements used in moisture simulations are approximately twice the maximum dimension of than those used in EIT). However, since the size of the elements in moisture simulations are already very small, further decrease of the element size would only minimally impact the moisture simulation results. It should be noted that since herein we only qualitatively compare the results of EIT with moisture flow simulations the difference in mesh size between EIT and moisture flow simulations does not impact the overall conclusions and findings of the work.

Figure 8 compares the EIT reconstructions from the two experiments: ingress of plain water (left column) and ingress of water with Iohexol (right column). The EIT images show a clear difference in the absorption rates of plain water and water with Iohexol. The size of the wetted volume is consistently larger in the images corresponding to ingress of plain water. Moreover, the values of the conductivity change $\delta\sigma$ are significantly higher in the left column of Figure 8 than in the respective images in the right column, suggesting significantly higher moisture content – and absorption rate – for plain water. In analyzing the raw measurement data, it was apparent that potential differences decrease with the ingress of moisture in the case of both Iohexol and plain water. However, due to the ill-posed nature of the EIT reconstruction problem, it is very difficult to draw quantitative conclusions from the raw data (small changes in potential measurements can correspond to very large differences in reconstructions due to the ill-posedness of the EIT inverse problem).

We would like to highlight that different scale bars are used in illustration of EIT reconstructions of specimens with Iohexol and plain water ingress. The different scales allow illustration of the regions of the moisture penetration in samples with Iohexol since they have approximately three time smaller conductivity change. We also would like to mention that the values of conductivity change in difference imaging scheme are qualitative due to the reasons discussed in Section 3.1. This means that the estimated change in conductivities do not necessary represent the actual conductivity change, rather a "larger change" in conductivity.

The results presented here indicate that EIT has enough spatial resolution to enable visualization of moisture and differentiate the flow rate of different fluids. Whereas X-ray CT could not be used to detect moisture movement, especially at low levels of saturation due to low contrast between the regions of varying moisture content at low moisture content levels. It should be noted that while EIT had sufficient resolution to image areas of low moisture content, X-ray CT could detect features that EIT could not. For example, in Figure 6 X-ray CT detected the large pores within the specimen due to contrast between the air and surrounding material. Such small features are generally difficult to detect with EIT, especially with difference imaging, since the scheme subtracts features present in the reference measurements. In principal, small features such as air voids, can be detected with absolute imaging provided they are within distinguishability limit and proper prior information is used.

The sorptivity test described in Section 2 resulted initial sorptivities of 0.38 $(\mathrm{mm}/\sqrt{\mathrm{hr}})$ for plain water and 0.31 $(\mathrm{mm}/\sqrt{\mathrm{hr}})$ for water with Iohexol, respectively, indicating an 18% decrease of the absorption rate with the addition of Iohexol to water. The result of the sorptivity test thus supports results of the EIT experiment. Therefore, although the difference reconstructions in EIT are often qualitative, they enable distinguishing between different rates of moisture flow in this experiment.

To better visualize the ability of EIT to image moisture flows in 3D, the reconstructions from the two sets of experiments are illustrated in the 3D images shown in Figure 9. Again, the images indicate higher absorption for plain water than for water with Iohexol. Both of the 22-hour reconstructions show artifacts discussed above. However, in the reconstruction corresponding to ingress of water with Iohexol, there are less artifacts.

The significant artifacts observed in the EIT reconstruction of plain water ingress after 22-hours may have resulted from the change in contact impedance. The contact impedance between the silver paint and the specimen can change due to moisture reaching to the electrode. Moreover, in difference imaging, the inaccuracies in estimating contact impedance, in general, cancel out in between the two measurement sets if the contact impedance remains the same. In this case, the presence of moisture changes the contact impedance and therefore their effect does not cancel out between the measurements. Another reason for these artifacts is the significant conductivity change from the reference state. In the difference imaging, global linearizion is used with the implicit assumption that the conductivity change with respect to the reference state is small (see Section 3.1). Therefore, when conductivity change is very large and encompasses a large portion of the domain, the assumptions of difference imaging are violated, resulting in the artifacts seen in late-stage ingress. In addition, while efforts were made to avoid drying of the sample during the experiments, some drying of the bottom of the specimen may have occurred during experimentation, resulting in a drop of conductivity.

5 Summary and Conclusions

In the present paper, we investigated (i) whether EIT can be used to monitor 3D moisture flow in cement-based materials containing aggregates, and (ii) whether EIT has adequate sensitivity to detect difference in the flow rate of fluids of differing viscosity and surface tension. We conducted an experimental study, where 3D moisture flow in cement-based mortar containing fine aggregates was imaged using EIT and X-ray Computed Tomography (CT). In EIT, the difference imaging scheme was selected to reconstruct the change of the electrical conductivity of mortar from a reference state, i.e., the state before the moisture ingress. Measurements were performed during the ingress of water without and with Iohexol, a radiocontrast agent that increased viscosity and surface tension. In the presence of Iohexol, the rate of moisture penetration was slower, which was confirmed by preforming a sorption test.

CT images were compared to EIT results; however, CT images showed only the highly-saturated region directly below the water reservoir. To facilitate the comparison of flow patterns including low levels of saturation, numerical simulation of moisture flow was chosen as an additional corroboration method. The qualitative comparison of the EIT reconstructions with the results of numerical simulation of unsaturated moisture flow shows that the EIT reconstructions agree with the results of simulations at early stages of moisture ingress. Moreover, the results show that EIT provides sufficient sensitivity to show differing flow rates of fluids with differing viscosity and surface tension. At later stages, significant artifacts appear in the reconstructions. Therefore, at later stages of moisture ingress, where the change in electrical conductivity may be larger, different imaging schemes in EIT may be needed. In conclusion, difference-imaging based EIT can provide a suitable non-destructive, non-invasive method of monitoring unsaturated 3D moisture flow in cement-based material at least at early stages of moisture ingress in cement-based materials containing aggregates.

References

Abramoff M, Magalhaes P, Ram S (2004) Image processing with ImageJ. Biol Med Phys Biomed 11(7):36–42
Adler A, Lionheart WR (2006) Uses and abuses of EIDORS: an extensible software base for EIT. Physiol Meas 27(5):S25
ASTM (2006) Standard practice for making and curing concrete test specimens in the laboratory
Auroy M, Poyet S, Le Bescop P, Torrenti JM, Charpentier T, Moskura M, Bourbon X (2015) Impact of carbonation on unsaturated water transport properties of cement-based materials. Cement Concrete Res 74:44–58
Bauters T, DiCarlo D, Steenhuis T, Parlange J (2000) Soil water content dependent wetting front characteristics in sands. J of Hydrol 232:244–254
Bear J (1988) Dynamics of fluids in porous media, 2nd edn. Dover Publications, Inc., New York
Beck A, Ben-tal A (2006) On the solution of the tikhonov regularization of the least squares problem. SIAM J of Optimiz 17(1):98–118
Borcea L (2002) Electrical impedance tomography. Inverse Probl 18:R99–R136
Borsic A, Comina C, Foti S, Lancellotta R, Musso G (2005) Imaging heterogeneities with electrical impedance tomography: laboratory results. Géotechnique 55(7):539–547
Bouchette G, Church P, Mcfee J, Adler A (2014) Imaging of compact objects buried in underwater sediments using electrical impedance tomography. Geosciences and Remote Sensing 52(2):1407 – 1417
Buettner M, Ramirez A, Daily W (1996a) Electrical resistance tomography for imaging concrete structures. In: Structural materials technology an NDT Conference, San Diego, California
Buettner M, Ramirez A, Daily W (1996b) Electrical resistance tomography for imaging the spatial distribution of moisture in pavement sections. In: Structural materials technology an NDT Conference, San Diego, California
Chen Q, Gingras M, Balcom B (2003) A magnetic resonance study of pore filling processes during spontaneous imbibition in Berea sandstone. J Chem Phys 119(18):9609–9616
Cheng KS, Isaacson D, Newell J, Gisser D (1989) Electrode models for electric current computed tomography. IEEE T Bio-Med Eng 36(9):918–924

Comina C, Cosentini R, Della Vecchia G, Foti S, Musso G (2010) Hydrochemomechanical processes in soil samples: moni-
toring through electrical resistivity tomography. In: EPJ Web of Conferences, EDP Sciences, vol 6, p 22012

Comina C, Cosentini RM, Della Vecchia G, Foti S, Musso G (2011) 3d-electrical resistivity tomography monitoring of salt
transport in homogeneous and layered soil samples. Acta Geotech 6(4):195–203

Cosentini RM, Della Vecchia G, Foti S, Musso G (2012) Estimation of the hydraulic parameters of unsaturated samples by
electrical resistivity tomography. Géotechnique 62(7):583–594

Daily W, Ramirez A, Binley A, Henry-Poulter S (1994) Electrical resistance tomography of concrete structures. In:
ECAPT94: 3rd European concerted action meeting on process tomography, Lisbon, Portugal

Deinert M, Parlange J, Steenhuis TJ T, Ünlü K, Cady K (2004) Measurement of fluid contents and wetting front profiles
by real-time neutron radiography. J of Hydrol 290(3-4):191–201

Dierke C, Werban U (2013) Relationships between gamma-ray data and soil properties at an agricultural test site. Geoderma
199:90–98

Dormieux L, Kondo D, Ulm F (2006) Microporomechanics, 1st edn. John Wiley & Sons, West Sussex, England

Du Plooy R, Villain G, Palma Lopes S, Ihamouten A, Dérobert X, Thauvin B (2015) Electromagnetic non-destructive
evaluation techniques for the monitoring of water and chloride ingress into concrete: a comparative study. Mater Struct
48(1):369–386

Duliu OG, Rizescu CT, Ricman C (2003) Dual energy gamma-ray axial computer tomography investigation of some meta-
morphic and sedimentary rocks. Neues Jahrbuch fòr Geologie und Paläontolgie 228:343–362

Feeman T (2010) The Mathematics of Medical Imaging, 1st edn. Springer Science, LLC., New York

Ford S, Shane J, Mason T (1998) Assignment of features in impedance spectra of the cement-paste/steel system. Cement
Concrete Res 28(12):1737–1751

Gélis C, Revil A, Cushing M, Jougnot D, Lemeille F, Cabrera J, De Hoyos A, Rocher M (2010) Potential of electrical
resistivity tomography to detect fault zones in limestone and argillaceous formations in the experimental platform of
Tournemire, France. Pure Appl Geophys 167(11):1405–1418

van Genuchten MT (1980) A closed-form equation for predicting the hydraulic conductivity of unsaturated soils. Soil Sci
Soc Am J 44:892–898

van Genuchten MT, Nielson DR (1985) On describing and predicting the hydraulic properties of unsaturated soils. Ann of
Geophys 3:615–628

Ghasemzadeh F, Pour-Ghaz M (2014) The effect of damage on moisture transport in concrete. J Mat Civil Eng pp DOI:
10.1061/(ASCE)MT.1943–5533.0001,211

Gummerson R, Hall C, Hoff W, Hawkes R, Holland G, Moore W (1979) Unsaturated water flow within porous materials
observed by NMR imaging. Nature 281:56–57

Haegel F, Zimmerman E, Esser O, Breede K, Huisman J, Glaas W, Berwix J, Vereecken H (2011) Determination of the
distribution of air and water in porous media by electrical impedance tomography and magneto-electrical imaging. Nuc
Eng D 241:1959–1969

Hall C, Hoff W (2012) Water transport in brick, stone and concrete, 2nd edn. Taylor & Francis, London and New York

Hallaji M (2015) Monitoring damage and unsaturated moisture flow in concrete with electrical resistance tomography
(ERT). Ph.D. thesis, North Carolina State University, Raleigh, North Carolina

Hallaji M, Seppänen A, Pour-Ghaz M (2014) Electrical impedance tomography-based sensing skin for quantitative imaging
of damage in concrete. Smart Mater Struct 23(8):085,001

Hallaji M, Seppänen A, Pour-Ghaz M (2015) Electrical resistance tomography to monitor unsaturated moisture flow in
cementitious materials. Cement and Concrete Res 69:10–18

Heidary-Fyrozjaee M (2008) Control of displacement fronts in porous media by flow rate partitioning. Ph.D. thesis, Uni-
versity of Southern California, Los Angeles, CA

Isaacson D (1986) Distinguishability of conductivities by electric current computed tomography. IEEE T Med Imaging
5(2):91–95

Jennings HM (2000) A model for the microstructure of calcium silicate hydrate in cement paste. Cement Concrete Res
30(1):101–116

Kaipio J, Somersalo E (2005) Statistical and Computational Inverse Problems. Springer New York

Kanematsu M, Maruyama I, Noguchi T, Iikura H, N T (2009) Quantification of water penetration into concrete through
cracks by neutron radiography. Nucl Instrum Methods Phys Res Sect A 605(1-2):154–158

Krautblatter M, Hauck C (2007) Electrical resistivity tomography monitoring of permafrost in solid rock walls. J Geophys
Res - Earth 112(F2)

Kuras O, Pritchard J, Meldrum P, Chambers J, Wilkinson P, Ogilvy R, Wealthall G (2009) Monitoring hydraulic processes
with automated time-lapse electrical resistivity tomography (ALERT). Appl Geophys 341:868–885

LaBrecque D, Ramirez A, Daily W, Binley AM, Schima S (1996) ERT monitoring of environmental remediation processes.
Meas Sci Technol 7(3):375

Leech C, Lockington D, Hooton R, Galloway G, Cowin G, Dux P (2008) Validation of Mualem's conductivity model and
prediction of saturated permeability from sorptivity. ACI Mater J 105(1):44–51

Looms MC, Jensen KH, Binley A, Nielsen L (2008) Monitoring unsaturated flow and transport using cross-borehole geo-
physical methods. Vadose Zone J 7(1):227–237

Masschaele B, Dierick M, Cnudde V, Van Hoorebeke L, Delputte S, Gildemeister A, Gaehler R, Hillenbach A (2004) High-
speed thermal neutron tomography for the visualization of water repellents, consolidants and water uptake in sand and
lime stones. Radiat Phys Chem 71(3):807–808

McCarter W (1996a) Monitoring the influence of water and ionic ingress on cover zone concrete subjected to repeated
absorption. Cement Concrete Aggr 18(1):55–63

McCarter W, Watson D (1997) Wetting and drying of coverzone concrete. In: Inst. Civ. Eng. Struct. Build., vol 112, pp
227–236

McCarter W, Ezirim H, Emerson M (1996b) Properties of concrete in the cover zone: Water penetration, sorptivity, and
ionic ingress. Mag Concrete Res 48(176):149–156

McCarter W, Chrisp T, Starrs G, Adamson A, Owens E, Basheer P, Nanukuttan S, Srinivasan S, Holmes N (2012) Devel-
opments in performance monitoring of concrete exposed to extreme environments. J Infrastruct Syst 18(3):167–175

Merz S, Polhmeier A, Vanderborght J, van Dusschoten D, Vereecken H (2014) Moisture profiles of the upper soil layer during evaporation monitored by NMR. Water Resour Res 50(6):51845195

MSDS (2016) Pelco electrically-conductive silver paint

Mualem Y (1976) A new model for predicting the hydraulic conductivity of unsaturated porous media. Water Resour Res 12(3):513–522

Nielsen A (1972) Gamma-ray-attenuation used for measuring the moisture content and homogeneity of porous concrete. Build Sci 7(4):257–263

Nimmer RE, Osiensky JL, Binley AM, Sprenke KF, Williams BC (2007) Electrical resistivity imaging of conductive plume dilution in fractured rock. Hydrogeol J 15(5):877–890

Nizovtsev M, Stankus S, Sterlyagov A, Terekhov V, RA K (2008) Determination of moisture diffusivity in porous materials using gamma-method. Int J Heat Mass Transf 54(17-18):4161–4167

Perlo J, Danieli E, Perlo J, Blümich B, Casanova F (2013) Optimized slim-line logging NMR tool to measure soil moisture in situ. J of Mag Res 233:74–79

Pires LF, Bacchi OO, Reichardt K (2005) Gamma ray computed tomography to evaluate wetting/drying soil structure changes. Nucl Instrum Meth B 229(3):443–456

Polydorides N, Lionheart W (2002) A matlab toolkit for three-dimensional electrical impedance tomography: a contribution to the electrical impedance and diffuse optical reconstruction software project. Meas Sci Technol 13(12):1871–1883

Pour-Ghaz M (2011) Detecting damage in concrete using electrical methods and assessing moisture movement in cracked concrete. Ph.D. thesis, Purdue University, Indiana

Pour-Ghaz M, Weiss J (2011) Detecting the time and location of cracks using electrically conductive surfaces. Cement Concrete Comp 33(1):116–123

Pour-Ghaz M, Rajabipour F, Couch J, Weiss J (2009) Numerical and experimental assessment of unsaturated fluid transport in saw-cut (notched) concrete elements. ACI Special Publication 266:73–86

Pour-Ghaz M, Spragg R, Weiss J (2010) Moisture profiles and diffusion coefficients in mortars containing shrinkage reducing admixtures. International RILEM Conference on Use of Superabsorbent Polymers and Other New Additives in Concrete Technical University of Denmark:197–206

Poyet S, Charles S, Honore N, L'hostit V (2011) Assessment of unsaturated water transport properties in an old concrete: determination of the pore-interaction factor. Cement and Concrete Res 41(10):1015–1023

Raoufi K, Schlitter J, Bentz D, Weiss J (2011) Parametric assessment of stress development and cracking in internally cured restrained mortars experiencing autogenous deformations and thermal loading. Advances in Civil Engineering 2011

Richards LA (1931) Capillary conduction of liquids through porous mediums. Physics 1(5):318–333

Richardson I (1999) The nature of CSH in hardened cements. Cem Concr Res 29(8):1131–1147

Roels S, Carmeliet J (2006) Analysis of moisture flow in porous materials using microfocus X-ray radiography. Int J Heat Mass Transf 49(25-26):4762–4772

Roels S, Carmeliet J, Hens H, Adan O, Brocken H, Cerny R, Pavlik Z, Ellis A, Hall C, Kumaran K (2004) A comparison of different techniques to quantify moisture content profiles in porous building materials. J Thermal Env and Bldg Sci 27(4):261–276

Schöberl J (1997) NETGEN an advancing front 2d/3d-mesh generator based on abstract rules. Computing and visualization in science 1(1):41–52

Slater L, Binley A, Versteeg R, Cassiani G, Birken R, Sandberg S (2002) A 3D ERT study of solute transport in a large experimental tank. J Appl Geophys 49(4):211–229

Smyl D, Ghasemzadeh F, Pour-Ghaz M (2015) Simulation of unsaturated moisture transport in damaged mortar and concrete. J of Mat Civil Eng (under review)

Smyl D, Hallaji M, Seppänen A, Pour-Ghaz M (2016) Three-dimensional electrical imaging of moisture ingress in mortar. ACI Special Publication

Somersalo E, Cheney M, Isaacson D (1992) Existence and uniqueness for electrode models for electric current computed tomography. SIAM Jour on Appl Math 52(4):1023–1040

Spragg RP, Castro J, Li W, Pour-Ghaz M, Huang PT, Weiss J (2011) Wetting and drying of concrete using aqueous solutions containing deicing salts. Cement and Concrete Comp 33(5):535–542

Stacey R (2006) Electrical impedance tomography, geothermal program interdisciplinary research in engineering and earth sciences. Tech. Rep. SGP-TR-182, Stanford University

Tiana I, Heck R, Elliot T (2007) Application of X-ray computed tomography to soil science:a literature review. Can J of Soil Sci 88(1):1–20

Tikhonov A, Arsenin V (1977) Solutions of Ill-posed Problems. John Wiley & Sons Inc

Ulm F, Constantinides G, Heukamp F (2004) Is concrete a poromechanics material? - a multiscale investigation of poroelastic properties. Mater Struct 37:43–58

Vauhkonen M, Vadasz D, Karjalainen PA, Somersalo E, Kaipio JP (1998) Tikhonov regularization and prior information in electrical impedance tomography. IEEE T Med Imaging 17(2):285–293

Vauhkonen M, Lionheart W, Heikkinen L, Vauhkonen P, Kaipio J (2001) A MATLAB package for the EIDORS project to reconstruct two-dimensional EIT images. Physiol Meas 22:107–111

Vauhkonen P (2004) Image reconstruction in three-dimensional electrical impedance tomography. PhD thesis, University of Kuopio

Vauhkonen PJ, Vauhkonen M, Savolainen T, Kaipio JP (1999) Three-dimensional electrical impedance tomography based on the complete electrode model. IEEE T Biomedical Eng 46(9):1150–1160

Villani C, Spragg R, Pour-Ghaz M, Weiss J (2014) The influence of pore solutions properties on drying in cementitious materials. J of the Am Ceram Soc 97:386–393

Vontobel P, Lehmann E, Carlson WD (2005) Comparison of X-ray and neutron tomography investigations of geological materials. IEEE T Nucl Sci 52(1):338–341

Šimůnek J, van Genuchten MT, Šejna M (2008) Development and applications of the HYDRUS and STANMOD software packages and related codes. Vadose Zone J 7(2):587–600

Weiss J, Pour-Ghaz M (2011) Application of frequency selective circuits for crack detection in concrete elements. Journal of ASTM International 8(10):1–11

Wildenschild D, Vaz C, Rivers M, Rikard D, Christensen B (2002) Using X-ray computed tomography in hydrology: systems, resolutions, and limitations. J Hydrol 267(3):285–297

Woracek R, Penumadu D, Kardjilov N, Hilger A, Boin M, Banhart J, Manke I (2014) 3d mapping of crystallographic phase distribution using energy-selective neutron tomography. Adv Mater 26(24):4069–4073

Zhang P, Wittmann F, Zhao T, EH L (2010) Neutron imaging of water penetration into cracked steel reinforced concrete. Physica B 405(7):1866–1871

Zhang P, Wittmann F, Zhao T, EH L, Vontobel P (2011) Neutron radiography, a powerful method to determine time-dependent moisture distributions in concrete. Nucl Eng Des 241(12):4758–4766

Zreda M, Desilets D, Ferré T, Scott R (2008) Measuring soil moisture content non-invasively at intermediate spatial scale using cosmic-ray neutrons. Geophys Res Lett 35:doi:10.1029/2008GL035,655
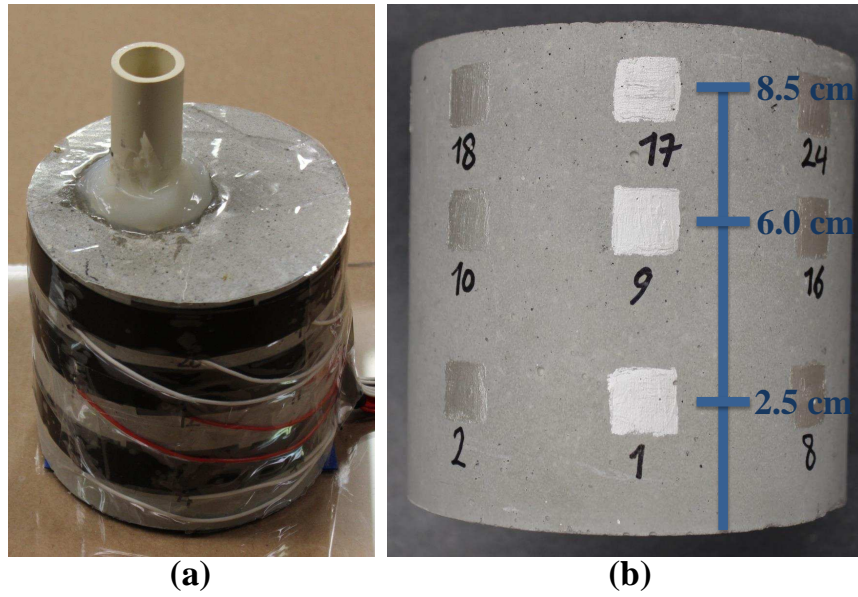
Fig. 1 (a) Prepared EIT specimen with PVC water reservoir, (b) mortar specimen and locations of the painted-silver electrodes
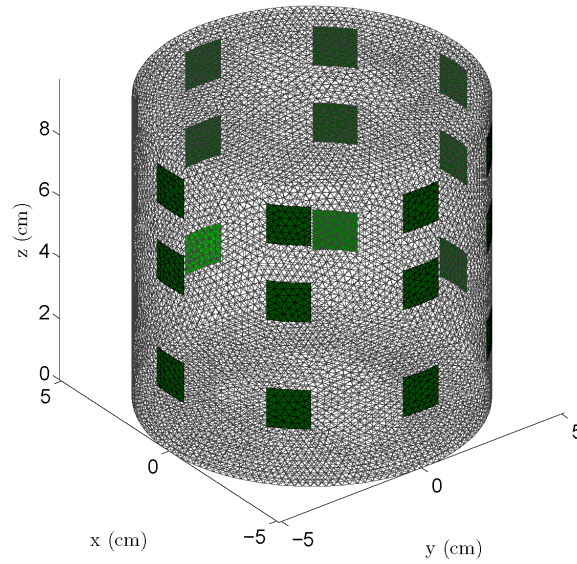
**Fig. 2** FEM mesh used in EIT reconstructions
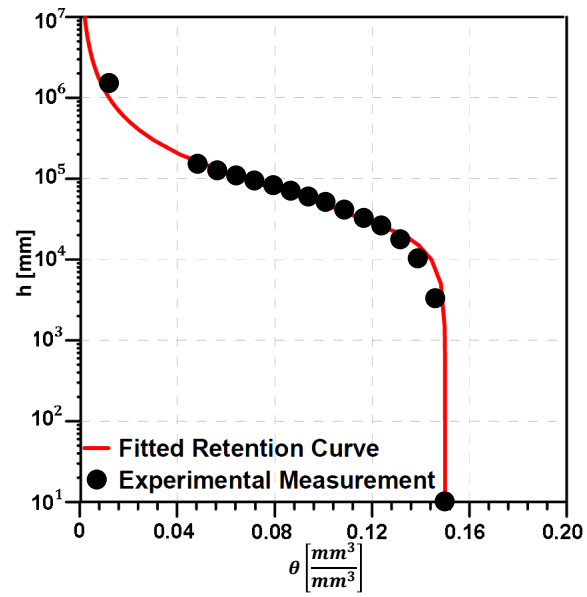
**Fig. 3** Fitted moisture retention curve for mortar using van Genuchten parameters
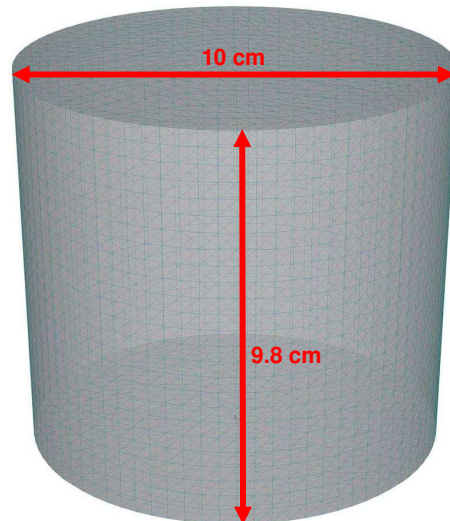

Fig. 4 FEM mesh used in moisture flow simulations
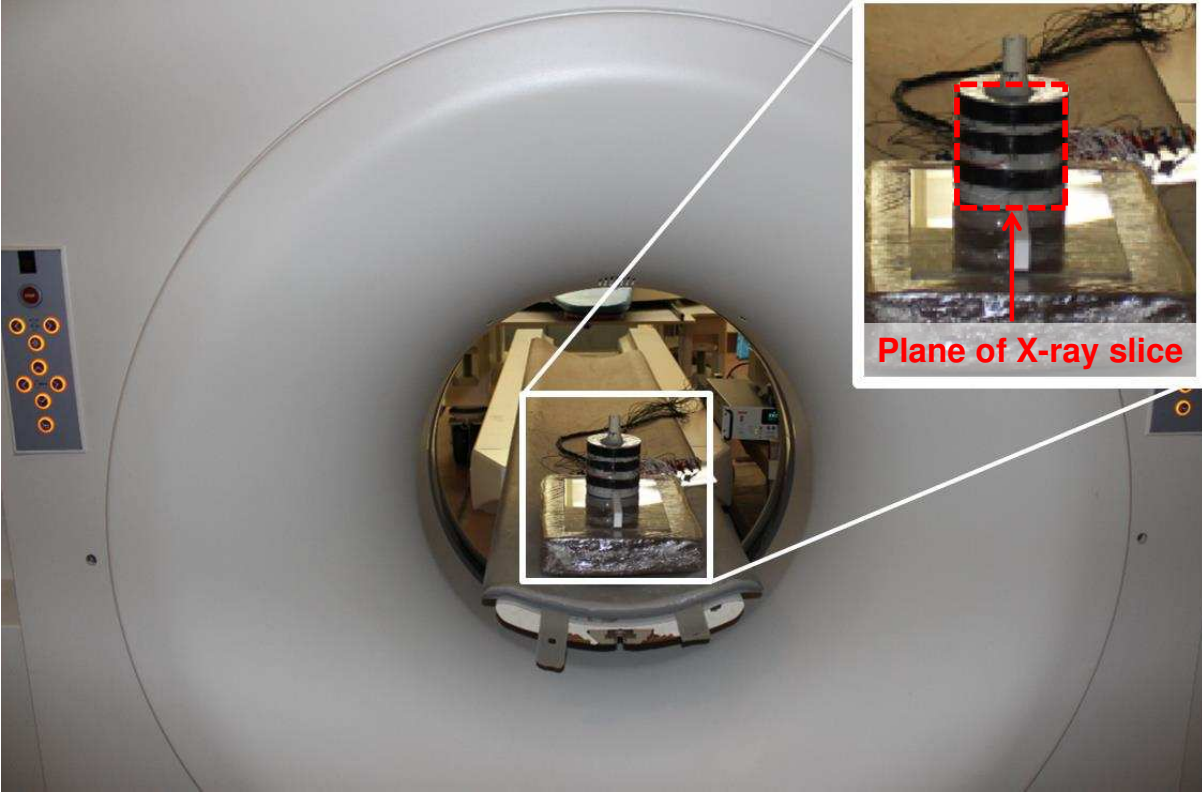
Fig. 5 Full-scale medical CT scanner with a peak beam energy of 120 kV and intensity of 40-200 mA testing the EIT specimen used in this study.
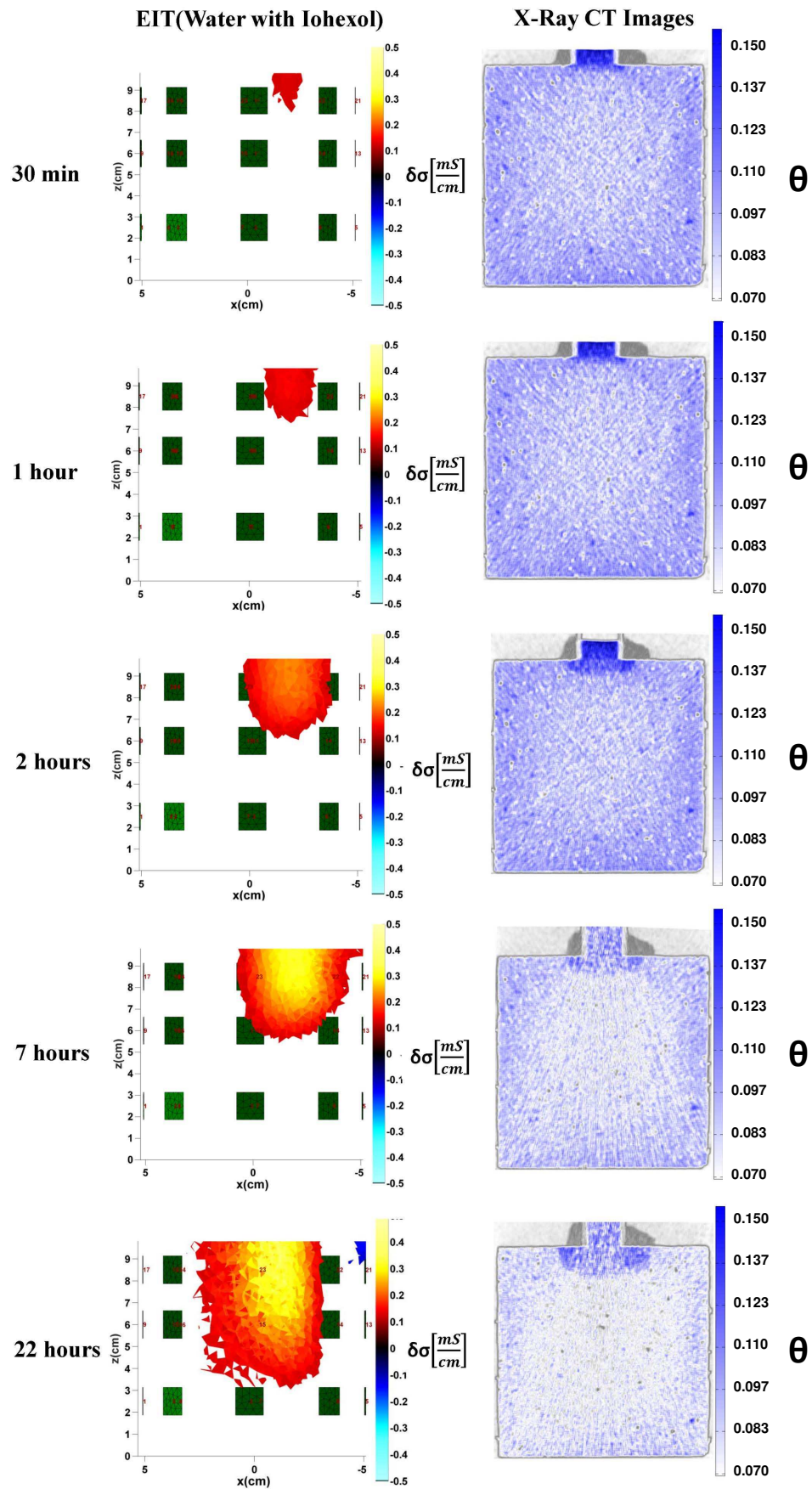
Fig. 6 Two-dimensional (2D) slices of the conductivity change based on 3D EIT reconstructions (left column), and CT images (right column) at different times of the moisture ingress (with radiocontrast agent, Iohexol).
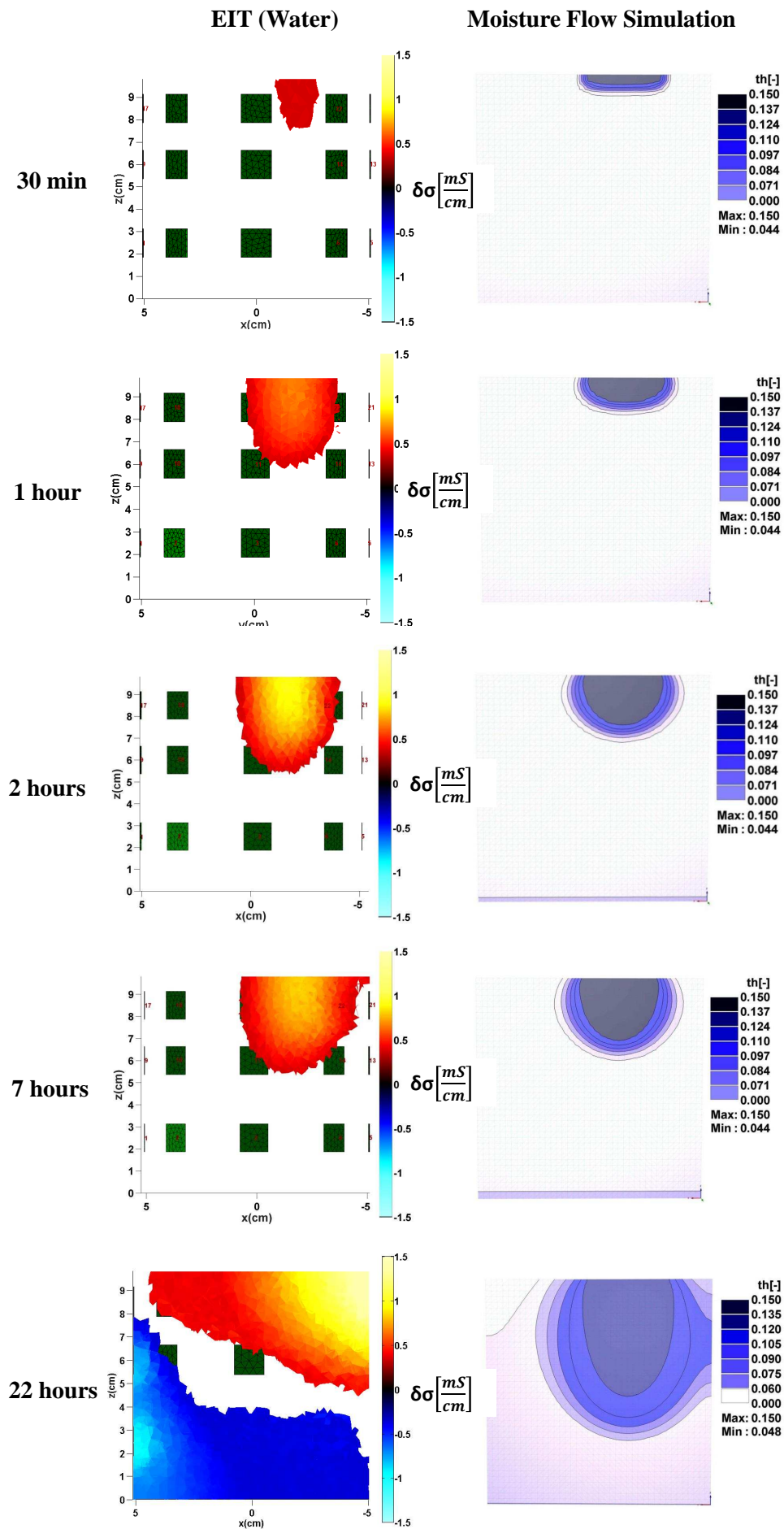
Fig. 7 Two-dimensional (2D) slices of the conductivity change based on 3D EIT reconstructions (left column), and unsaturated moisture flow simulations (right column) at different times of the moisture ingress.
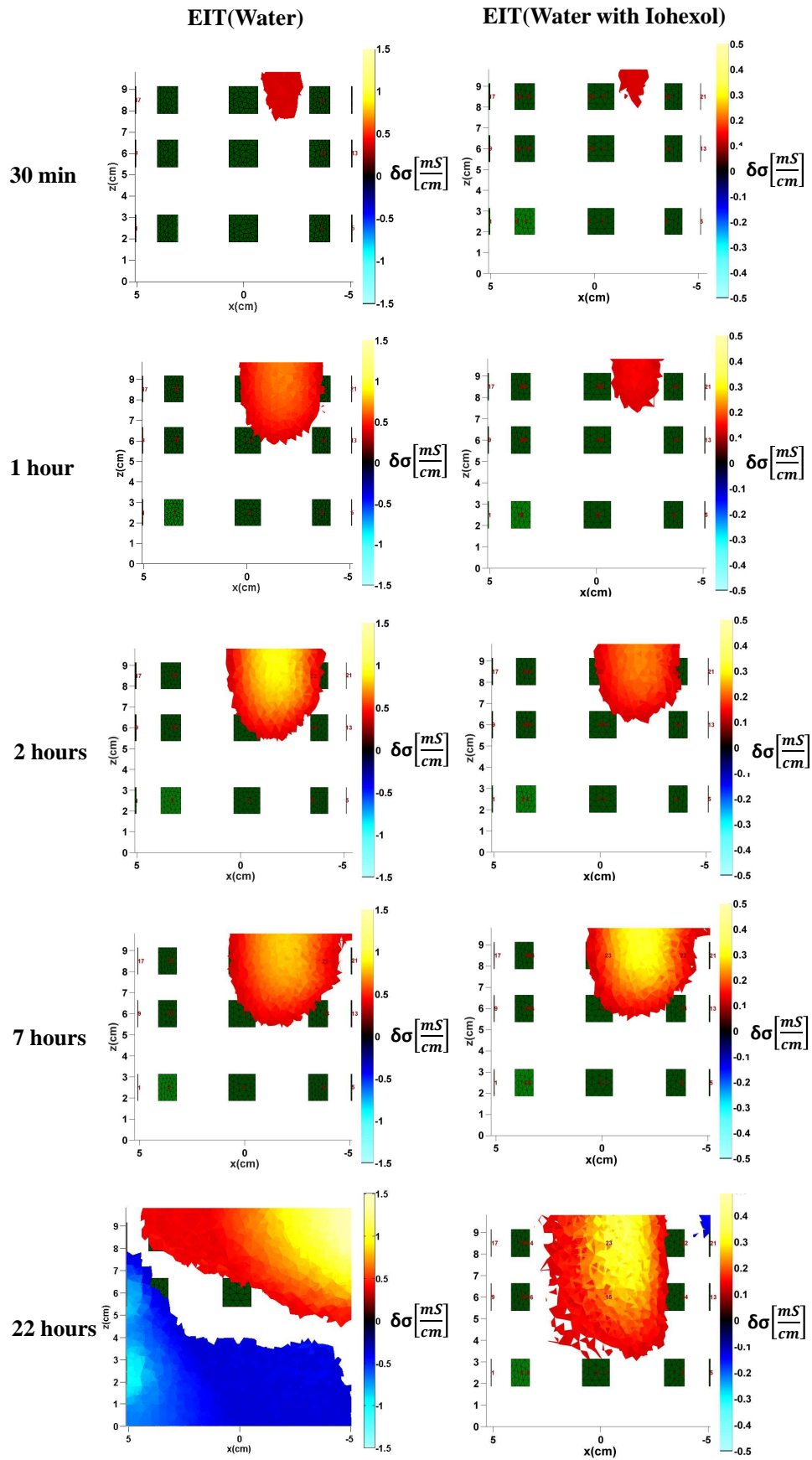
Fig. 8 Two-dimensional (2D) slices of the conductivity change based on 3D EIT reconstructions for water (left column), and two-dimensional (2D) slices of the conductivity change based on 3D EIT reconstructions for water with Iohexol (right column).
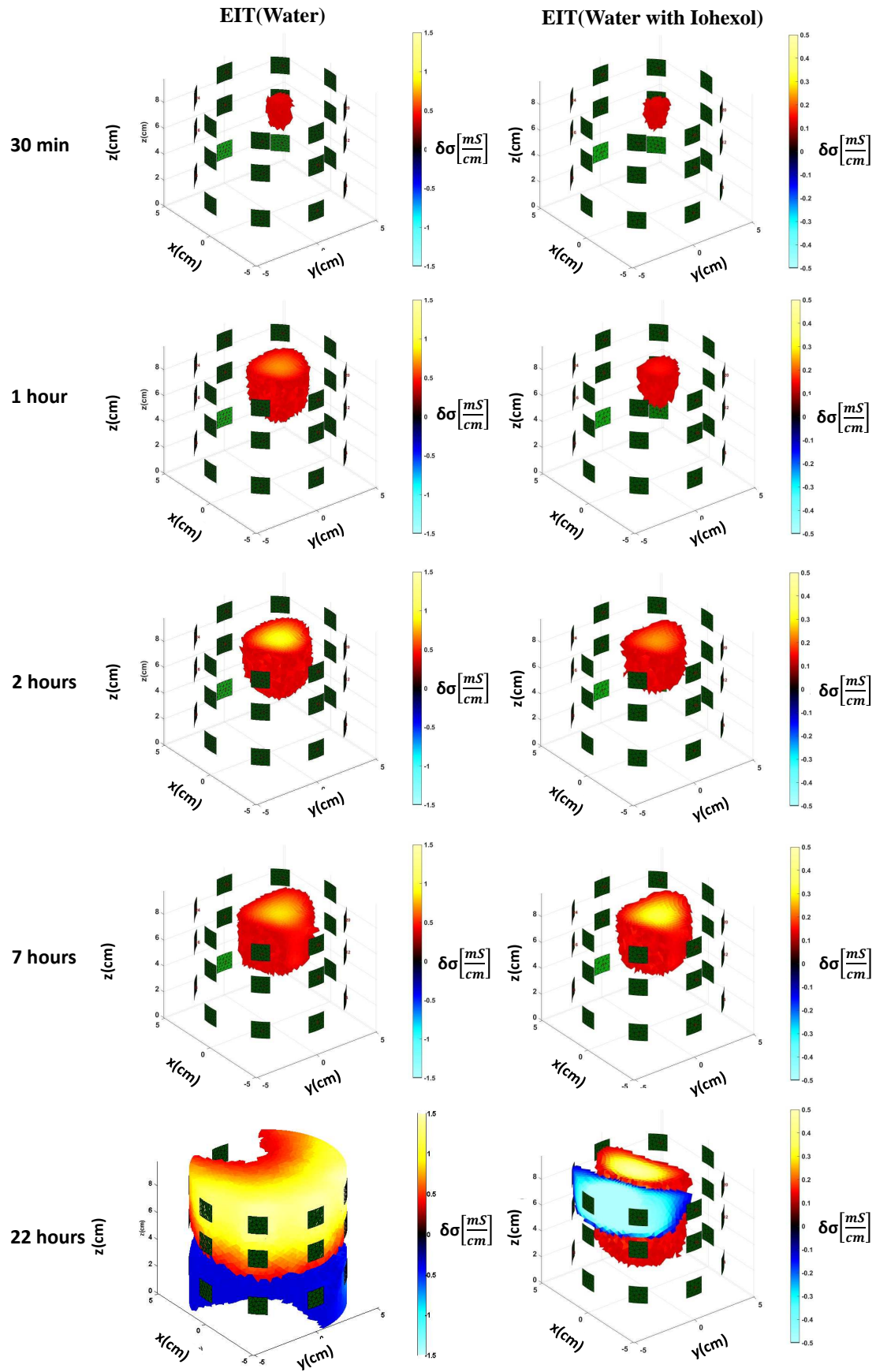
Fig. 9 3D EIT reconstructions of conductivity change for water (left column), and 3D EIT reconstructions of conductivity change for water with Iohexol (right column).